The Astrophysical Journal, 777:54 (14pp), 2013 November 1 doi:10.1088/0004-637X/777/1/54

DISSOCIATIVE RECOMBINATION MEASUREMENTS OF HCl^+ USING AN ION STORAGE RING

O. Novotný[1], A. Becker[2], H. Buhr[2], C. Domesle[2], W. Geppert[3], M. Grieser[2], C. Krantz[2], H. Kreckel[2], R. Repnow[2], D. Schwalm[2,4], K. Spruck[5], J. Stützel[1], B. Yang[2,6], A. Wolf[2], and D. W. Savin[1]
[1] Columbia Astrophysics Laboratory, Columbia University, New York, NY 10027, USA; oldrich.novotny@mpi-hd.mpg.de
[2] Max Planck Institute for Nuclear Physics, D-69117 Heidelberg, Germany
[3] Department of Physics, Stockholm University, AlbaNova, SE-106 91 Stockholm, Sweden
[4] Department of Particle Physics and Astrophysics, Weizmann Institute of Science, Rehovot 76100, Israel
[5] Institut für Atom- und Molekülphysik, Justus-Liebig-Universität Giessen, D-35392 Giessen, Germany
[6] Institute of Modern Physics, Chinese Academy of Sciences, Lanzhou 730000, China
Received 2013 May 31; accepted 2013 July 10; published 2013 October 17

ABSTRACT

We have measured dissociative recombination (DR) of HCl^+ with electrons using a merged beams configuration at the TSR heavy-ion storage ring located at the Max Planck Institute for Nuclear Physics in Heidelberg, Germany. We present the measured absolute merged beams recombination rate coefficient for collision energies from 0 to 4.5 eV. We have also developed a new method for deriving the cross section from the measurements. Our approach does not suffer from approximations made by previously used methods. The cross section was transformed to a plasma rate coefficient for the electron temperature range from $T = 10$ to 5000 K. We show that the previously used HCl^+ DR data underestimate the plasma rate coefficient by a factor of 1.5 at $T = 10$ K and overestimate it by a factor of three at $T = 300$ K. We also find that the new data may partly explain existing discrepancies between observed abundances of chlorine-bearing molecules and their astrochemical models.

Key words: astrochemistry – ISM: clouds – ISM: molecules – methods: laboratory: molecular – molecular data – molecular processes

1. INTRODUCTION

Despite the fact that the elemental abundance of chlorine is orders of magnitude lower than that of more abundant elements such as carbon or oxygen, astrochemists have been interested in chlorine chemistry for nearly 40 years now. The evolving understanding of Cl in the interstellar medium (ISM) can be followed in a series of papers over this time (e.g., Jura 1974; Dalgarno et al. 1974; Blake et al. 1986; Federman et al. 1995; Amin 1996; Sonnentrucker et al. 2006; Neufeld & Wolfire 2009; Lis et al. 2010; De Luca et al. 2012; Neufeld et al. 2012). A surprising development in this is that, in spite of the low cosmic abundance of Cl, the latest observations indicate that the abundances of chlorine-containing molecules can be comparable to those of H_2O or CH (Lis et al. 2010; Neufeld et al. 2012).

Until recently, only one chlorine-bearing molecule had been observed in the ISM, namely HCl (Peng et al. 2010 and references therein). With the advent of the *Herschel Space Observatory*, H_2Cl^+ and HCl^+ ions have also been detected (Lis et al. 2010; De Luca et al. 2012). This allows for a much more detailed comparison of astrochemical models to the observations. The H_2Cl^+ abundances derived from these observations are over 10 times greater than those of the latest models (Neufeld et al. 2012). Similarly, the observed HCl^+ abundance is several times larger than predicted by models (Neufeld & Wolfire 2009). One possible candidate for explaining these discrepancies would be an erroneous rate coefficient for dissociative recombination (DR) of HCl^+ assumed in the models. For a detailed description of the Cl chemistry, see the review by Neufeld & Wolfire (2009). To highlight the importance of HCl^+ within the chlorine ISM chemistry, we discuss a few of the key reactions in the network.

With a value of 12.97 eV, the ionization potential of Cl lies slightly below that of atomic hydrogen. Thus, in the illuminated portions of interstellar clouds, photoionization of neutral atomic H does not shield neutral atomic Cl from the interstellar radiation field. As a result, atomic chlorine is predominantly found in the form of Cl^+. The uniqueness of chlorine astrochemistry is due to the exoergic formation of HCl^+ via

$$Cl^+ + H_2 \rightarrow HCl^+ + H. \quad (1)$$

All other elements predominantly found in interstellar clouds as singly charged atomic ions react endoergically with H_2. Once HCl^+ is formed it can react exoergically with H_2 to create H_2Cl^+ via

$$HCl^+ + H_2 \rightarrow H_2Cl^+ + H. \quad (2)$$

Neutral HCl is then formed, in part, by DR of H_2Cl^+ through

$$e^- + H_2Cl^+ \rightarrow H + HCl. \quad (3)$$

However, HCl^+ can also undergo DR via

$$e^- + HCl^+ \rightarrow H + Cl. \quad (4)$$

This reaction reduces the HCl^+ abundance, slowing the formation of H_2Cl^+ and HCl via Reactions (2) and (3), and thereby affecting their equilibrium abundances.

To the best of our knowledge, there have been no previous investigations into DR of HCl^+ until recently (e.g., our experimental work and exploratory theoretical studies by Larson et al. 2012). Lacking reliable data, astrochemical models have used a "typical" diatomic DR rate coefficient for that of HCl^+. It has been shown, however, that DR rate coefficients of diatomics can differ by large factors from alleged typical values. For example, for CF^+ Novotny et al. (2005) measured a rate coefficient a factor of four lower than that commonly taken for the typical diatomic ion value. For this reason, Neufeld et al. (2012) have identified the DR rate coefficient of HCl^+ as an "urgently needed" parameter significantly affecting the uncertainty of chlorine-chemistry models.

To meet these needs, we have carried out DR measurements for HCl^+. The DR pathways relevant for HCl^+ are described in Section 2. The experimental setup, measurement method, and data analysis are discussed in Section 3 of this paper. In Section 4, we present the resulting merged beams DR rate coefficient for HCl^+, derive a DR cross section and, subsequently, the Maxwellian plasma DR rate coefficient. We discuss our results and their implications for astrochemistry in Section 5. A summary is given in Section 6.

2. DR PATHWAYS FOR HCl^+

In any DR process the incident electron couples within the Franck–Condon region of the initial ionic state to form an excited neutral state (Larsson & Orel 2008). This may autoionize back to form a molecular ion again, or it can dissociate into neutral DR products.

Depending on the nature of the excited neutral state into which the incident electron is captured, two basic types of DR can be distinguished (e.g., Larsson & Orel 2008). In direct DR this neutral state is electronically doubly excited and repulsive so that the molecule can directly dissociate. The range of electron energies accessible for the transition within the Franck–Condon region is given by the steepness of the neutral doubly excited state involved. Usually this range is large and results in broad structures in the DR cross-section spectrum. Alternatively, the incident electron can be captured into a bound neutral state. Such levels have discrete total energies and give rise to sharp resonances in the energy dependence of the DR cross section as their predissociation contributes to DR. This process is called indirect DR. The dissociation in both DR types can induce multiple transitions between the electronic states.

The neutral bound levels involved in indirect DR can often be grouped into various Rydberg series. Members of a given series differ by the excitation level n of the captured electron. Each such series converges as $n \rightarrow \infty$ to a single bound level of the ionic core with specific rotational, vibrational, and electronic quantum numbers. In general, with increasing collision energy for a given Rydberg series, the density of the neutral states increases and then drops to zero above the series limit. DR resonances from this indirect recombination process may be experimentally unresolvable as they can overlap due to their natural widths and also due to the limited experimental energy resolution. However, what may still be experimentally distinguishable is a change in the DR cross section at the end of a neutral Rydberg series, i.e., at the electron–ion collision energy corresponding to the specific excitation of the ionic core. This change could be either an increase or decrease, depending on the specific pathways involved as well as potential quantum mechanical interferences (Larsson & Orel 2008). The DR cross section may also drop above an ionic core excitation limit because electron impact excitation of the ion competes with DR occurring at energies above this limit.

Quantum interferences between neutral states belonging to various excitation channels may also lead to unexpected structures in the DR spectrum. Further discussion can be found, for example, in Larsson & Orel (2008), Wolf et al. (2011), and Waffeu Tamo et al. (2011). Lacking detailed information on these mechanisms for neutral levels lying in the HCl^+ electronic scattering continuum, we use the location of the ionic excitation thresholds and of the main dissociation curves as a guide.

The basic properties of HCl^+ DR can be obtained from its thermochemistry. We can calculate the exothermicity for DR of HCl^+ in the ground $X\,^2\Pi_{3/2}$ state using the ~13.6 eV ionization energy of the hydrogen atom and the ~5.3 eV proton affinity of chlorine (Linstrom & Mallard 2013). For collisions at $E = 0$ this exothermicity results in an energy release of ~8.3 eV. This is less than the $\gtrsim$8.9 eV and $\gtrsim$10.2 eV energies needed to electronically excite Cl and H, respectively (Ralchenko et al. 2011). Hence, low-energy DR of HCl^+ results in both atomic products being exclusively in their ground states. As the exothermicity is insufficient to internally excite the DR products, it goes instead into the kinetic energy released (KER), which is carried away by the products. The channels with excited Cl, excited H, or both become accessible only for $E \gtrsim 0.6$ eV, 1.9, and 2.5, respectively.

DR of multielectron systems such as HCl^+ is a complex process that involves a large number of resonances in the electron scattering continuum. The molecular structure of HCl^+ and HCl determine the behavior of the DR cross section versus electron–ion collision energy E. The most likely dissociative route from potential energies near the HCl^+ ground state toward the H and Cl ground states is via the HCl repulsive $^3\Sigma^+$ potential curve. This curve crosses the HCl^+ ground state potential curve at internuclear distances somewhat smaller than the Franck–Condon region of the $HCl^+(v = 0)$ initial state (Bettendorff et al. 1982). Thus, low-energy DR here is most likely driven by the indirect process. In the first step the electron is captured to one of the ro-vibrationally excited neutral levels converging to an excited HCl^+ core. This then couples to the $^3\Sigma^+$ repulsive potential curve and predissociates. Data on molecular levels formed by optical excitation of HCl to states near (but below) the ionization threshold for forming HCl^+ are available from spectroscopic and theoretical studies (e.g., Bettendorff et al. 1982; Liyanage et al. 1995; Alexander et al. 1998; Romanescu & Loock 2007; Lefebvre-Brion et al. 2011; Long et al. 2013).

Based on the above discussion, structures in the energy dependence of the DR cross section may occur near HCl^+ excitation thresholds. For ground state $X\,^2\Pi_{3/2}$ HCl^+, some of these limits are rotational excitations, fine-structure $X\,^2\Pi_{3/2} \rightarrow X\,^2\Pi_{1/2}$ excitation, and vibrational excitations. Another series worth mentioning may arise from electronic excitation of HCl^+ into the $A^2\Sigma^+$ state.

Electron-induced processes that could compete with DR and thus reduce the DR signal are all endothermic. One of these is ion pair formation which can yield H^++Cl^- or H^-+Cl^+ at energies above 1.7 eV and 3.9 eV, respectively. Another electron-driven process is dissociative excitation (DE) forming H + Cl^+ or H^+ + Cl. This reaction is endothermic by ~4.7 eV and ~5.3 eV, respectively.

3. EXPERIMENTAL

3.1. Setup

Measurements were carried out at the TSR heavy-ion storage ring of the Max Planck Institute for Nuclear Physics in Heidelberg, Germany (Habs et al. 1989). With a base pressure of $\sim 10^{-11}$ mbar, TSR is ideally suited to simulate the two-body collision regime important for interstellar gas-phase chemistry. Details on various aspects of the merged beams technique as used at TSR and the recent developments of the photocathode electron beam and the fragment imaging technique have been described by Amitay et al. (1996), Krantz et al. (2009), and Novotný et al. (2010). Here we discuss only those aspects specific to this study.

HCl^+ ions were produced in a cold-cathode Penning ion source from a mixture of H_2 and HCl parent gases. Ions were extracted from the source and brought to a kinetic energy of 2.4 MeV using a Pelletron-type accelerator. The magnetically mass-filtered beam of $^1H^{35}Cl^+$ was then selected for and injected into TSR where it was stored for ∼33 s.

The stored ion beam was merged for ∼1.5 m with a nearly monoenergetic electron beam. This beam, which we refer to as the Target, is generated by a photocathode operated at temperatures of around 100 K (Orlov et al. 2004, 2005, 2009), thereby enabling us to perform electron–ion collision studies with high-energy resolution (Sprenger et al. 2004). After ion injection at time $t = 0$ and continuing until $t = 16$ s, the electron beam was velocity matched to the ions. During this time elastic collisions of the ions with the low energy spread (i.e., cold) electron beam transferred energy from the circulating ions to the single-pass electrons. This mechanism of electron cooling of the ions, also known as phase-space cooling (Poth 1990), results in reducing the ion beam velocity spread and a reduced ion beam diameter.

The ion beam energy of 2.4 MeV was limited by the highest available magnetic field strength available for deflecting the stored ions along the orbit within TSR. Velocity matching the electrons with the 36 amu HCl^+ ions resulted in an electron beam energy as low as 36.9 eV. Under these conditions, obtaining a phase-space cooled ion beam requires an electron beam of both high density and low temperature. Such a beam was achieved by utilizing the cryogenically cooled photocathode electron source in the Target which provided an electron density of $n_e \approx 2 \times 10^6$ cm^{-3} and a low energy spread as we discuss below. The cooling capability of the Target for high-mass ions was demonstrated previously for a beam of 31 amu CF^+ ions (Krantz et al. 2009). In the present measurement, in spite of the low electron energy and high ion mass, an ion beam diameter as low as 0.5 mm was obtained. The second electron beam device of the TSR, referred to as the Cooler (Steck et al. 1990), proved to have insufficient cooling force to cool such heavy, slow molecular beams within the available storage time. Therefore the Cooler was not used for the results presented here.

After cooling, the Target electron beam was used as the interaction medium to measure HCl^+ DR for a range of electron–ion center-of-mass collision energies by varying the laboratory energy of the electron beam. Neutral DR products generated in the Target were not deflected by the first dipole magnet downstream of its position in TSR and continued ballistically until they hit a detector. Data were collected with this detector from $t = 16$ s to $t = 33$ s as described in Section 3.3.

The energy spread of the photocathode-generated electron beam is parameterized by effective temperatures $T_\perp$ and $T_{||}$, perpendicular and parallel to the bulk electron beam velocity, respectively. The magnetic field guiding the electrons was higher at the photocathode, compared to the interaction zone, by a factor of $\xi = 20$ for most of the measurements. This expansion of the magnetic field leads to a lowering of the perpendicular electron temperature (Danared 1993; Orlov et al. 2005). By fitting dielectronic recombination resonances (Lestinsky et al. 2008) and from fragment imaging spectra obtained at similar values of ξ (Stützel 2011), we deduce effective temperatures of $k_B T_\perp = 1.65 \pm 0.35$ meV and $k_B T_\parallel = 25^{+45}_{-5}$ μeV for the present measurement, where k_B is the Boltzmann constant. Here and throughout the rest of this paper, all uncertainties are quoted at an estimated 1σ statistical confidence level. Some of the data were also acquired with an expansion factor of $\xi = 40$, for which

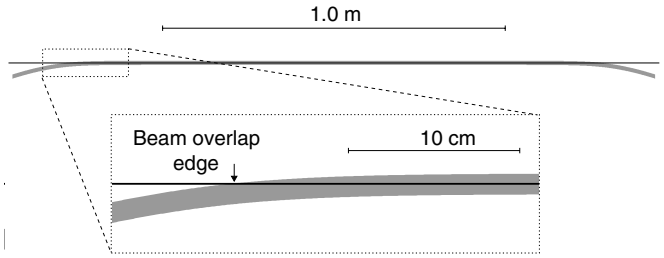

Figure 1. Top-down view of the geometry in the Target for the electron beam (gray line) and ion beam (black line). This geometry was used in the Monte Carlo simulation to generate the energy distribution f_{mb}. The image inset shows the detail of the electron beam merging region. The system possesses mirror symmetry around a plane passing through the center of the Target and perpendicular to both beams.

a reduced transverse electron temperature of $k_B T_\perp \approx 0.83$ meV is estimated, while $k_B T_{||}$ is expected to remain unchanged (e.g., Danared 1993). The relevant temperatures $k_B T_\perp$ and $k_B T_\parallel$ enter the data analysis as described in Section 3.4.

The interaction geometry is determined by the shapes of the overlapping electron and ion beams. The electron beam geometry is determined by the magnetic fields in the Target (Sprenger 2003). The electron beam can be treated as a cylindrical body, bent at the ends, with a diameter d_e given by the product of the cathode size and the square root of the expansion factor ξ. This yields $d_e = 12.6$ mm and 17.8 mm for $\xi = 20$ and 40, respectively. The cooled ion beam diameter d_i is typically less than 0.5 mm. The electron and ion beam geometries are shown in Figure 1 and are discussed in more detail in the Appendix.

The fact that the electron beam is significantly wider than the ion beam enabled the complete spatial overlap of the ion beam by the electrons in the interaction region. We optimized the alignment of the beams by minimizing the time needed for phase-space cooling of the beam (Hochadel et al. 1994). Better alignment gives a better overlap, thereby reducing the required cooling time. Observationally, we monitored the necessary cooling time and beam size either using a beam profile monitor (Hochadel et al. 1994) or by examining the center of mass for DR events as projected on the multichannel plate (MCP) imaging detector (Amitay et al. 1996; Krantz et al. 2009).

The bulk electron beam energy in the laboratory frame, E_{meas}, is needed to calculate the center-of-mass electron–ion collision energy during the measurement. We determine E_{meas} from the measured cathode voltage by correcting it for the space charge of the electron beam (Kilgus et al. 1992). This correction requires knowing the electron density profile, which we measured with the method described in Sprenger et al. (2004). The electron density is expected to be homogeneous along the beam axis.

3.2. HCl^+ Internal Excitation

The HCl^+ ions produced in the discharge are expected to initially possess electronic, vibrational, rotational, and fine-structure excitation. We estimate that much of this internal excitation radiatively relaxes during the 16 s of electron cooling. Electronically, the only known HCl^+ metastable state below the dissociation limit is the $A\,^2\Sigma^+$ which lies ∼3.6 eV above the $X\,^2\Pi$ ground state. Measured and calculated radiative lifetimes for $A\,^2\Sigma^+ \rightarrow X\,^2\Pi$ transitions are shorter than ∼3.4 μs (Pradhan et al. 1991 and references therein). The known radiative lifetimes for vibrational relaxation of the $X\,^2\Pi$ electronic ground state span from ∼4.9 ms for $v = 1 \rightarrow 0$ to ∼1.3 ms for $v = 9 \rightarrow 8$ (Pradhan et al. 1991). Higher vibrational levels are expected to

decay even faster. Thus we expect the stored ions to cascade quickly to their ground electronic and vibrational levels.

We predict that the rotational lifetimes are sufficiently short so that during the initial phase most of the rotations J will have radiatively relaxed and come into equilibrium with the ~300 K black body radiation of the vacuum chamber. We have calculated the rotational radiative lifetimes of $X\,^2\Pi_{3/2}(v = 0)$ for levels ranging from $J = 3/2$ to $J = 51/2$. In actuality, we could truncate the calculations at $J = 20/2$, as the higher levels decay so rapidly that they do not affect the precision of the model. Our approach uses a method similar to that of Amitay et al. (1994). The static dipole moment for HCl^+ was taken from Cheng et al. (2007). The dominant emission lines are expected to be $J \rightarrow J - 1$. Restricting ourselves to these transitions, we have built a relaxation model using the spontaneous radiative decay lifetimes along with stimulated emission and absorption by the 300 K black body radiation. For the initial rotational excitation we have taken a Boltzmann distribution at a temperature of 8000 K. This is approximately the excitation temperature derived for CF^+ produced in the same ion source (Novotný et al. 2009). After the initial 16 s of ion storage, the predicted average excitation energy exceeds the 300 K equilibrium by only 10%. The excitation energy averaged over the ion population during the $t = 16$–33 s measurement window exceeds room temperature excitation by only 3%. This predicted level of excitation might be slightly overestimated due to the omission of spin-orbit coupling which may provide extra decay pathways. We have also not accounted for the possible additional acceleration of the rotational cooling from super-elastic ion collisions with electrons (e.g., Shafir et al. 2009).

The one type of excitation that is unlikely to relax during ion storage is the fine-structure splitting of the $X\,^2\Pi_{3/2-1/2}$, which amounts to ~80 meV (Sheasley & Mathews 1973). We are unaware of any published lifetime estimates for this transition. However, for a rough estimate we can use the radiative lifetime of the fine-structure excited $J = 1/2$ level in the isoelectronic atomic system Ar^+ with an energy of ~165 meV. That lifetime is calculated to be 23.7 s (Fischer & Tachiev 2013). Since the radiative decay rate of this magnetic dipole transition scales as the third power of the transition frequency, then leaving aside the details of the transition matrix element, we expect that the lifetime of the corresponding level in the HCl^+ molecular state will be longer by almost an order of magnitude. Hence, the $X\,^2\Pi_{1/2}$ radiative lifetime is expected to significantly exceed the ion storage time here.

3.3. Measurement Procedure

Data acquisition began after the 16 s period of injection and cooling was completed. During data acquisition the Target beam energy was stepped repeatedly between *cooling*, *measurement*, *reference*, and *off* (all defined below). The time durations were 35, 25, 25, and 25 ms, respectively. An additional 5 ms delay before each step was added to allow the power supplies to reach the desired voltage. This cycle was repeated 130 times for a total of ~17 s.

For the first step, cooling, the electrons were velocity matched to the ions at an electron energy of $E_{\rm cool} = 36.91$ eV in the laboratory frame. These interleaved cooling steps ensured a constant phase-space spread of the ions during data acquisition.

In the second step, measurement, the electron beam energy was detuned, giving a mean energy of $E_{\rm meas}$ in the laboratory frame. The nominal center-of-mass collision energy can then readily be calculated from the mean electron and ion velocities in the laboratory frame. This yields what we call the detuning energy

$$E_{\rm d} = \left(\sqrt{E_{\rm meas}} - \sqrt{E_{\rm cool}}\right)^2. \quad (5)$$

The detector count rate in this step was used to determine the merged beams rate coefficient versus $E_{\rm d}$. The detuning energy was changed for each new ion injection.

The third step, reference, was included as a cross check and for normalization. The energy in this step was set to a constant value of $E_{\rm d} = 0.019$ eV. The resulting signal was used to monitor the ion beam intensity.

In the last step, off, the electron beam was not admitted into the interaction region. The resulting background signal was due solely to ion interactions with the residual gas inside TSR.

DR events were measured using a 10×10 cm^2 Si surface-barrier detector located ~12 m downstream of the Target. Fragments from a given dissociation event arrived at the detector with only a few nanoseconds difference in flight times. This is shorter than the detector time resolution and so only one pulse was counted for each dissociation event, independent of the number of products reaching the detector. The high exothermicity of HCl^+ DR results in relative fragment kinetic energies of up to KER $\approx$ 8.3 eV. This can cause a large displacement between the fragments when reaching the detector. The resulting positions of some of the H fragments exceeded the size of the detector. The heavier Cl fragments, however, were confined to a narrow cone and 100% of the DR-generated Cl struck the detector. We verified this using an MCP-imaging technique (e.g., Amitay et al. 1996). Thus, to achieve essentially 100% DR event counting efficiency, we derive our signal from the count of detector events independent of the number of fragments detected in each of them.

The detector count rate consisted of both DR and background events. The dominant source of this background was collisions of ions with residual gas. We have corrected for these events by taking the count rate at measurement and subtracting the count rate acquired with the electron beam off. Our approach does not account for potential background due to non-DR, but this is expected to be negligible at the energies studied (Krauss & Julienne 1973; Dalgarno & Black 1976; Larsson & Orel 2008). Additional background due to electron-driven DE forming $H^+ + Cl$ was not an issue as the measured collision energies were all significantly below the DE threshold of 5.3 eV.

The measured relative merged beams DR rate coefficient is determined by normalizing the recorded DR signal by the electron density and ion number (e.g., Amitay et al. 1996). The electron beam density is well determined by the measured beam current, energy, and geometry (Sprenger et al. 2004). However, the maximum stored HCl^+ ion current of $I_{\rm i} < 1\,\mu$A was too low to be determined directly using a DC current transformer. Instead we used a measurement of the relative ion beam intensity by taking the detector signals from the reference and off steps as proxies for the relative ion beam intensity. This allows us to normalize our measured data to obtain a relative merged beams DR rate coefficient versus $E_{\rm d}$. The whole curve was then scaled using an absolute measurement of the merged beams DR rate coefficient at matched electron and ion velocities (i.e., $E_{\rm d} = 0$ eV). Here we used an independent method based on precise ion beam storage lifetime measurements with and without the electron beam present in the interaction zone (Novotný et al. 2012). This method requires using the length of the beam interaction region, which was determined from the known beam geometries to be $L = 1.570$ m.

In the past, researchers have corrected the merged beams DR rate coefficient for the effects from the merging and demerging of the electron beam with the stored ions (Lampert et al. 1996). Below we introduce a new data analysis method which avoids the necessity of this correction.

3.4. Generating a Plasma DR Recombination Rate Coefficient

Using storage ring results, one can generate a DR rate coefficient suitable for a plasma with a Maxwell–Boltzmann collision energy distribution. This involves deconvolving the measured DR data to remove the effects of the experimental electron velocity spread and the beam overlap geometry. Mowat et al. (1995) and Lampert et al. (1996) have presented approximate methods for addressing these two issues. The resulting cross section can then be convolved with a Maxwell–Boltzmann distribution to generate a plasma rate coefficient suitable for astrochemical modeling. Here we have developed a more precise method for deriving the cross section which avoids making the approximations used by Mowat et al. and Lampert et al.

3.4.1. Measured Merged Beams DR Rate Coefficient

Experimentally we have measured a merged beams DR rate coefficient $\alpha_{\rm mb}$ which is given by

$$\alpha_{\rm mb}(E_{\rm d}) = \int \sigma(E)\, v\, f_{\rm mb}(E, E_{\rm d}, T_{||}, T_{\perp}, \boldsymbol{X})\, dE. \qquad (6)$$

Here σ is the DR cross section, E and v are the center-of-mass electron–ion energy and the relative velocity, respectively, and $f_{\rm mb}$ is the center-of-mass energy spread taking into account both the electron beam energy spread and the experimental geometry. The relationship between the collision energy and velocity is given by $E = \frac{1}{2}\,\mu\, v^2$, where μ is the reduced mass of the collision system. The large mass difference between the electron and ion allows us to set $\mu = m_e$. The term $f_{\rm mb}$ is a function of the detuning energy; the electron energy spread, which is given by the effective temperatures $T_{\perp}$ and $T_{\|}$; and the overlap geometry between the beams, symbolically represented as $\boldsymbol{X}$.

For parallel ion and electron beams, the velocity spread can be described by a "flattened" Maxwellian distribution in the center-of-mass frame. This velocity distribution is discussed in more detail by Andersen et al. (1989) and Poth (1990), while the corresponding energy distribution function is described by Schippers et al. (2004). Note that a pre-factor of $\frac{1}{2}$ is missing from Equation (1) given in Schippers et al.

In the merging and de-merging regions of the Target, the energy distribution is additionally distorted due to the beams no longer running co-linearly. Lampert et al. (1996) discuss the corresponding increase of collision energies, assuming that $T_{\perp} = T_{||} = 0$. We are not aware, however, of an analytical representation of $f_{\rm mb}$ which accounts for the effects of both the velocity spread and the full overlap geometry. To address this issue, we have developed a numerical method for describing such an energy distribution which we discuss below.

3.4.2. Limitations of Previous Methods for Extracting a DR Cross Section

The traditional methods for deconvolving the cross section from the merged beams rate coefficient first correct the measured data for the overlap geometry effects using, for example, the method of Lampert et al. (1996). The corrected data are then treated as if the beams are parallel with an energy distribution $f^*_{\rm mb}$, giving

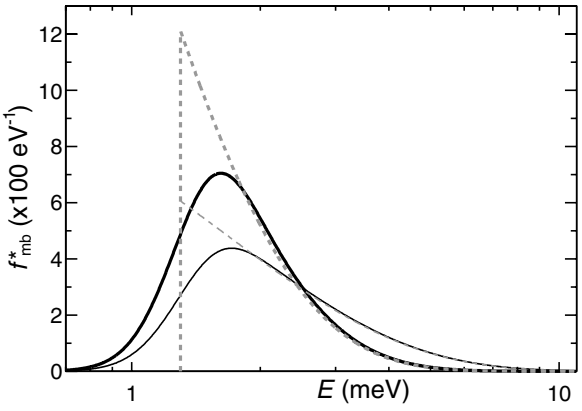

Figure 2. Collision energy distribution $f^*_{\rm mb}$ for parallel electron and ion beams at a detuning of energy $E_{\rm d} = 1.3$ meV. The black full curves use the Target longitudinal electron beam energy spread of $k_{\rm B}T_{\|} = 25\,\mu$eV. The gray dashed curves are for $k_{\rm B}T_{\|} = 0$. The thin curves assume a transverse electron energy spread of $k_{\rm B}T_{\perp} = 1.650$ meV, while the thick curves use $k_{\rm B}T_{\perp} = 0.825$ meV.

$$\alpha^*_{\rm mb}(E_{\rm d}) = \int \sigma(E)\, v\, f^*_{\rm mb}(E, E_{\rm d}, T_{||}, T_{\perp})\, dE. \qquad (7)$$

The analytic form of $f^*_{\rm mb}$ is given by Schippers et al. (2004) and the characteristic experimental energy spread in $f^*_{\rm mb}$ corresponds to (Müller 1999)

$$\Delta E \approx \sqrt{(k_{\rm B}T_{\perp}\, \ln 2)^2 + 16 \ln 2\, k_{\rm B}T_{\|}\, E_{\rm d}}. \qquad (8)$$

For high energies, where $E_{\rm d} \gg k_{\rm B}T_{\perp}$, the relative width $\Delta E/E_{\rm d}$ decreases to a small value. In that case, $f^*_{\rm mb}$ can often be approximated by a delta function $\delta(E - E_{\rm d})$. Equation (7) then collapses to $\alpha^*_{\rm mb}(E_{\rm d}) = \sigma(E_{\rm d})\, v$, and the cross section simplifies to

$$\sigma(E_{\rm d}) = \alpha^*_{\rm mb}(E_{\rm d}) \sqrt{\frac{m_e}{2E_{\rm d}}}. \qquad (9)$$

The situation is not so simple for $E_{\rm d} \lesssim k_{\rm B}T_{\perp}$. This regime is particularly critical for obtaining an accurate plasma rate coefficient at the low temperatures relevant to the cold ISM. At these low detuning energies, the cross section can be approximately derived using a method introduced by Mowat et al. (1995). Their technique makes use of the fact that typically $k_{\rm B}T_{\perp} \gtrsim 50\, k_{\rm B}T_{\|}$ in ion storage ring experiments. They go on to neglect the longitudinal energy spread by setting $k_{\rm B}T_{\|} = 0$. This makes ΔE and the shape of $f^*_{\rm mb}$ independent of $E_{\rm d}$ and one can then deconvolve $\alpha^*_{\rm mb}$ using Fourier analysis.

However, the approach of Mowat et al. raises a number of issues. Their method ignores the fraction of electron–ion collision energies E lying below $E_{\rm d}$. This can be seen in Figure 2 which shows the energy distribution function $f^*_{\rm mb}$ using two sets of Target electron temperatures. As a representative detuning energy we have chosen $E_{\rm d} = 1.3$ meV, which corresponds to a typical particle energy at molecular cloud temperatures of 10 K. In Figure 2, we also plot $f^*_{\rm mb}$ for the two Target values of $k_{\rm B}T_{\perp}$ but with $k_{\rm B}T_{\|} = 0$. These energy distributions clearly differ from those using a realistic $k_{\rm B}T_{\|} = 25\,\mu$eV. In $f^*_{\rm mb}(k_{\rm B}T_{\|} = 0)$ there is no collision energy population below $E_{\rm d}$. For $f^*_{\rm mb}(k_{\rm B}T_{\|} = 25\,\mu$eV) and an assumed value of $k_{\rm B}T_{\perp} = 1.65$ meV (0.825 meV), about 5% (10%) of the distribution is shifted to below $E_{\rm d}$. This fraction increases for

decreasing $k_B T_\perp / k_B T_\parallel$ or with increasing E_d, further reducing the validity of setting $k_B T_\parallel = 0$ in order to extract cross sections. Additionally, the potential errors in this method may increase if the cross section at low energies is highly structured or increases rapidly with decreasing energy. By using an energy distribution function which does not accurately represent the experimental conditions, the deconvolutions can accordingly under- or overestimate the cross section at a given value of E_d.

3.4.3. New Method for Extracting a DR Cross Section

The approach we use here is to create an empirical model cross-section spectrum $\sigma'(E)$ and, following Equation (6), convolve it with f_{mb} to generate a model experimental rate coefficient α'_{mb}. We represent $\sigma'(E)$ using a histogram-shaped function with an energy binning comparable to the energy resolution ΔE at E as given by Equation (8) with $E = E_d$. The amplitudes within each bin are treated as free fitting parameters and adjusted iteratively to minimize the χ^2 between the model α'_{mb} and the measured α_{mb}. The combined effects of the electron beam energy spread and the overlap geometry are treated using a Monte Carlo simulation of f_{mb} for the integration of Equation (6). In some cases (especially when the bin size becomes smaller than the energy resolution), the resulting $\sigma'(E)$ can fluctuate significantly from one to the next bin due to numerical instabilities. The corresponding uncertainties, however, essentially cancel out when integrating the cross-section to generate a plasma rate coefficient as described below. This method accounts for both the electron energy spread and the beam overlap geometry. Thus, our deconvolution method does not require the measured merged beams rate coefficient be corrected for the overlap geometry, nor is it based on the assumption that $k_B T_\parallel = 0$. In contrast to the traditional methods, we thereby largely avoid the uncertainties introduced by those assumptions. Technical details of our method are discussed at length in the Appendix.

3.4.4. Derived Plasma DR Rate Coefficient

Using the extracted $\sigma'(E)$ as a representation of $\sigma(E)$, we can generate a rate coefficient for a plasma with a thermal Maxwell–Boltzmann distribution f_{pl}. The resulting rate coefficient as a function of the plasma temperature T is given by

$$\alpha_{pl}(T) = \int \sigma(E)\, v\, f_{pl}(E, T)\, dE. \quad (10)$$

The analytical form of $f_{pl}(E, T)$ is well known and numerical integration of Equation (10) is straightforward.

3.5. Uncertainties in the Measured Merged Beams DR Rate Coefficient

The dominant uncertainty in the measured merged beams DR rate coefficient is derived from the ion beam storage lifetime measurements used to put the experimental results on an absolute scale. This error amounts to 11%. Additional minor sources of error arise from the electron density evaluation (∼4%) and the uncertainty on the electron beam geometry within the Target (≲2%). The total systematic uncertainty for the absolute scaling is then 12%.

The statistical uncertainty of each data point is given by the counting statistics for the number of signal and background counts. At collision energies $E_d < 10$ meV, this error amounts to ∼5%. At higher energies, this error increases as the signal and background become comparable. The statistical error is ∼45% at $E_d \approx 0.1$ eV and grows up to ∼200% at $E_d \approx 1$ eV.

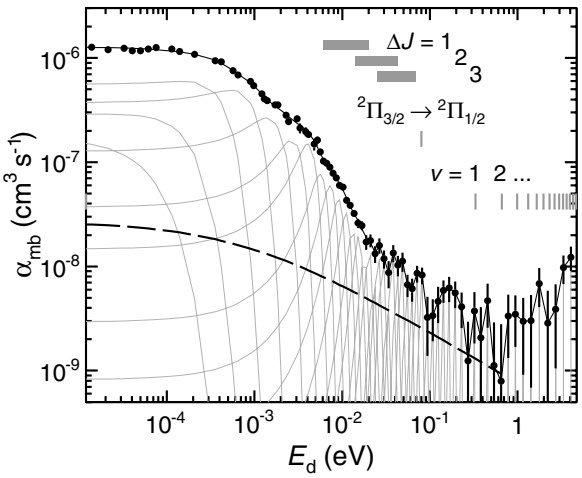

Figure 3. Experimental merged beams rate coefficient α_{mb} for DR of HCl^+ acquired with an adiabatic magnetic expansion factor of $\xi = 20$. The full circles show the data and the error bars indicate the 1σ statistical confidence level. Some of the error bars are smaller than the diameter of the plotted data points. The long dashed line illustrates the shape of the merged beams rate coefficient expected for direct DR, i.e., for $\sigma(E) \propto E^{-1}$, and is arbitrarily scaled on the vertical axis. To determine the cross section σ', the model rate coefficient α'_{mb} (black full line) was fitted to α_{mb}. The gray curves indicate the best fit sub-functions $\sigma'_i \Psi_i$, each corresponding to an individual convolved cross-section bin. See the Appendix for more details. The gray bars mark the range of rotational excitation thresholds with changes of angular momentum $\Delta J = 1$, 2, and 3 for initial levels from $J = 3/2$ to $J = 15/2$, i.e., the levels dominantly populated at 300 K. The fine-structure transition energy and the vibrational excitation thresholds are shown with vertical gray lines. All energies are given with respect to the HCl^+ ($X\,^2\Pi_{3/2}$) ground state.

4. RESULTS

4.1. Merged Beams Recombination Rate Coefficient

Figure 3 presents our merged beams rate coefficient for DR of HCl^+. These data are also given in tabular form in Table 1 . The error bars show the 1σ counting statistics. The detuning energy ranges from $E_d = 12\,\mu$eV to 4.5 eV. The data were acquired with $\xi = 20$ and cover the storage times of 16–33 s.

Although our model for the rotational relaxation of HCl^+ discussed in Section 3.1 indicates that most of the ions are in thermal equilibrium with the black body radiation of the TSR chamber, a small amount of rotational relaxation may still occur during the measurement period. To test for any effect of this cooling, we split the acquired data into two sets covering the storage times of 16–24 s and 24–33 s and analyzed these data sets independently. DR rate coefficients typically depend on the rotational excitation of the parent ions (Larsson & Orel 2008). Hence any significant change in rotational population should be observable in the DR rate coefficient spectra. However, to within their statistical uncertainties, the resulting two data sets for α_{mb} were equal at all values of E_d. This strongly suggests that the rotational excitation of the ions reached equilibrium with the black body radiation of the vacuum chamber during the initial electron cooling phase.

A possible source of concern in storage ring merged beams experiments is that the low energy α_{mb} can potentially be distorted if the ion beam energy is dragged by the detuned electron beam. The derivation of E_d through Equation (5) rests on the assumption of a constant mean ion beam velocity which is matched to the mean electron beam velocity at cooling. This assumption breaks down if, during the measurement step, the ion beam is dragged toward the detuned electron beam velocity

Table 1
Experimental Merged Beams Rate Coefficient α_{mb} for DR of HCl^+

E_d (eV)	α_{mb} ($cm^3\ s^{-1}$)	Statistical Error ($cm^3\ s^{-1}$)
1.39(−5)	1.27(−6)	6.15(−8)
2.13(−5)	1.20(−6)	3.79(−8)
3.27(−5)	1.24(−6)	5.46(−8)
4.05(−5)	1.17(−6)	5.62(−8)
5.00(−5)	1.17(−6)	4.88(−8)
6.16(−5)	1.22(−6)	6.81(−8)
7.59(−5)	1.26(−6)	6.39(−8)
1.14(−4)	1.22(−6)	5.18(−8)
1.40(−4)	1.16(−6)	4.28(−8)
2.07(−4)	1.08(−6)	3.93(−8)
3.56(−4)	9.41(−7)	3.23(−8)
4.20(−4)	9.22(−7)	5.04(−8)
5.69(−4)	7.55(−7)	2.57(−8)
6.51(−4)	6.85(−7)	4.03(−8)
9.04(−4)	5.94(−7)	2.06(−8)
9.83(−4)	5.43(−7)	3.13(−8)
1.21(−3)	4.54(−7)	2.26(−8)
1.30(−3)	4.04(−7)	2.11(−8)
1.39(−3)	3.90(−7)	2.82(−8)
1.72(−3)	3.55(−7)	2.20(−8)
1.84(−3)	3.56(−7)	1.81(−8)
2.28(−3)	2.83(−7)	1.85(−8)
2.45(−3)	2.45(−7)	1.43(−8)
3.05(−3)	2.61(−7)	1.27(−8)
3.29(−3)	2.12(−7)	2.40(−8)
3.82(−3)	1.97(−7)	1.93(−8)
4.12(−3)	1.84(−7)	1.26(−8)
4.81(−3)	1.49(−7)	1.89(−8)
5.21(−3)	1.63(−7)	1.32(−8)
5.64(−3)	1.25(−7)	8.80(−9)
6.11(−3)	1.02(−7)	4.52(−9)
6.64(−3)	9.76(−8)	3.68(−9)
7.21(−3)	8.92(−8)	3.68(−9)
7.85(−3)	7.84(−8)	3.71(−9)
8.56(−3)	7.05(−8)	3.03(−9)
9.36(−3)	5.99(−8)	2.89(−9)
1.02(−2)	5.77(−8)	3.04(−9)
1.12(−2)	4.32(−8)	2.86(−9)
1.24(−2)	3.86(−8)	2.84(−9)
1.36(−2)	3.23(−8)	2.39(−9)
1.51(−2)	2.60(−8)	2.67(−9)
1.68(−2)	2.47(−8)	2.46(−9)
1.87(−2)	1.71(−8)	2.74(−9)
2.10(−2)	1.78(−8)	2.50(−9)
2.36(−2)	1.32(−8)	2.42(−9)
2.66(−2)	1.59(−8)	2.62(−9)
3.00(−2)	1.19(−8)	2.36(−9)
3.38(−2)	8.71(−9)	2.51(−9)
3.82(−2)	1.35(−8)	2.49(−9)
4.32(−2)	1.03(−8)	2.31(−9)
4.89(−2)	1.12(−8)	2.36(−9)
5.55(−2)	6.68(−9)	1.63(−9)
6.30(−2)	6.10(−9)	1.51(−9)
7.17(−2)	8.58(−9)	1.59(−9)
8.18(−2)	8.26(−9)	1.52(−9)
9.36(−2)	3.24(−9)	1.85(−9)
1.07(−1)	3.37(−9)	1.46(−9)
1.24(−1)	4.63(−9)	1.76(−9)
1.43(−1)	5.91(−9)	1.45(−9)
1.66(−1)	6.23(−9)	1.69(−9)
1.95(−1)	5.59(−9)	1.60(−9)
2.29(−1)	4.09(−9)	1.53(−9)
2.71(−1)	1.24(−9)	1.70(−9)
3.21(−1)	3.74(−9)	1.93(−9)
3.81(−1)	2.07(−9)	2.01(−9)
4.53(−1)	4.70(−9)	2.13(−9)
5.41(−1)	1.12(−9)	1.79(−9)
6.48(−1)	7.94(−10)	2.00(−9)
7.81(−1)	3.34(−9)	2.02(−9)
9.46(−1)	3.49(−9)	1.80(−9)
1.15(+0)	2.96(−9)	2.05(−9)
1.42(+0)	3.01(−9)	2.32(−9)
1.77(+0)	6.86(−9)	2.78(−9)
2.20(+0)	2.86(−9)	2.99(−9)
2.72(+0)	3.89(−9)	2.85(−9)
3.34(+0)	9.75(−9)	2.97(−9)
4.06(+0)	1.23(−8)	3.20(−9)

Notes. The format $x(y)$ signifies $x \times 10^y$. There is an additional systematic uncertainty of 12% in the merged beams rate coefficient (see the text).

by dynamical friction forces of the same type as those causing electron cooling (Poth 1990). The actual collision energy is then smaller than that deduced from Equation (5). Since low-energy DR for HCl^+ increases with decreasing energy, this will enhance the measured signal at higher energies over what one would expect if there were no dragging. This will appear in the data as a broadening of α_{mb} close to 0 eV. In order to exclude such an experimental artifact, we have performed a series of tests described below. Based on these studies, we believe the ion beam dragging is not an issue in our experiment and that the low-energy shape in α_{mb} is due solely to DR.

The stability of the ion beam energy was tested by varying the duration of the various steps in the data cycle. The standard data cycle was chosen to optimize the duty factor and cooling as well as reduce dragging effects. All of the tests in this paragraph further improved cooling and reduced any potential dragging effects, but at the expense of significantly decreasing the measurement duty factor. The cooling step was lengthened by a factor of ∼3 to provide additional cooling and improve the ion beam stability. The measurement step was shortened from 25 ms to 10 ms to reduce any dragging effects. Additionally, we varied the energy difference between the reference step and the cooling step. If cooling were insufficient this would help to further minimize the dragging of the ion beam energy when at reference. To within the statistical accuracy of the measurement, all of these tests produced an α_{mb} that agreed with the data obtained under standard measurement conditions. Thus dragging of the ion beam energy does not appear to contribute to the observed low-energy rate coefficient.

To further test the DR origin of the low-energy data, we have measured the behavior of $\alpha_{mb}(E_d)$ for two different energy spreads. As one reduces the width of the collisional energy distribution, this results in a higher amplitude for α_{mb} at $E_d \sim 0$ eV after averaging over the electron energy distribution. Dragging, on the other hand, modifies only the width of the low-energy DR spectrum, not the peak amplitude. Here we narrowed the experimental energy spread by increasing the adiabatic expansion factor of the magnetic guiding field in the Target electron gun from $\xi = 20$ to $\xi = 40$. The transverse temperature is expected to scale as ξ^{-1}. Figure 4 presents both the $\xi = 20$ and $\xi = 40$ results. The higher expansion data do indeed show an additionally increased amplitude of the rate

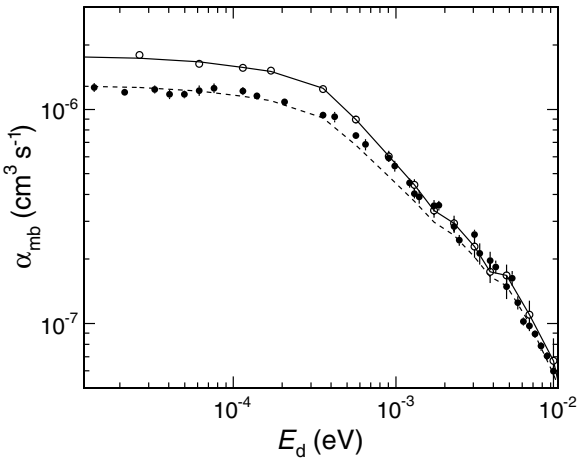

Figure 4. Experimental HCl^+ DR rate coefficients for adiabatic magnetic expansion factors of $\xi = 40$ and $\xi = 20$ are plotted by the open and full circles, respectively. The solid line shows the fit $\alpha'_{mb}(\xi = 40)$ while the dashed line is the converted $\alpha''_{mb}(\xi = 20)$ based on $\xi = 40$ data. See Section 4.1 for details.

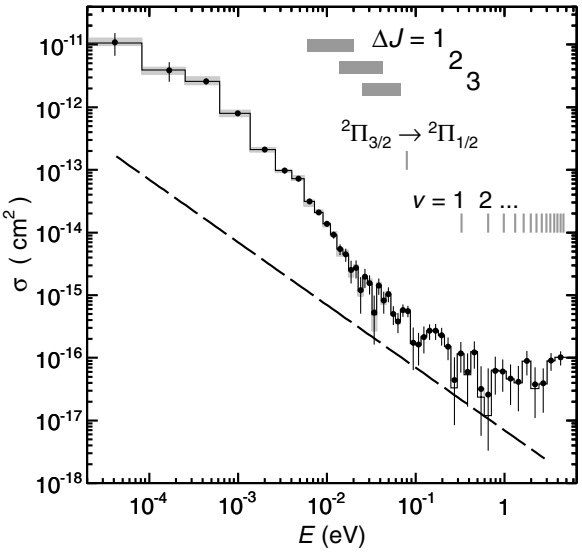

Figure 5. DR cross section for HCl^+ shown by the solid line histogram. The non-displayed lower edge of the left-most energy bin is at $E = 0$. The vertical error bars display the standard deviation of cross-section values obtained from deconvolving 1000 simulated merged beams rate coefficients. A full explanation is given in Section 4.2. The gray bars along the data show the error originating from uncertainties in $k_B T_\perp$ and $k_B T_\parallel$. The long-dashed line illustrates the shape of the merged beams rate coefficient expected for the direct DR process, i.e., $\sigma(E) \propto E^{-1}$. The curve is arbitrarily scaled on the vertical axis. The rotational, fine-structure, and vibrational thresholds are the same as in Figure 3.

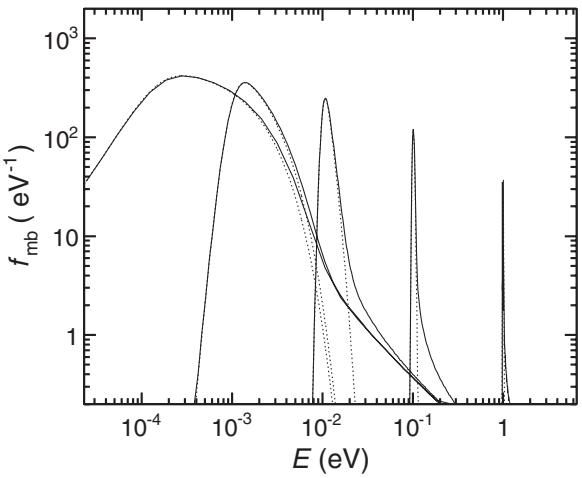

Figure 6. Simulated energy distribution functions f_{mb} (full line) for $E_d = 10^{-4}$ eV, 10^{-3} eV, 10^{-2} eV, 10^{-1} eV, and 1 eV (from left to right) for electron beam parameters $k_B T_\perp = 1.65$ meV, $k_B T_\parallel = 25\,\mu$eV, and the electron beam geometry of the Target. For comparison, we plot the energy distribution functions for parallel beams f^*_{mb} (dotted line). All f^*_{mb} functions are scaled so that the maxima match those of the corresponding f_{mb} functions.

coefficient at $E_d \lesssim 1$ meV. The half-width at half-maximum of the data below ~1 meV also narrowed by ~17%. This strongly suggests that the observed low-energy rate coefficient is caused by the DR process and not by beam dragging artifacts.

Still, the higher amplitudes in the low-energy $\alpha_{mb}(\xi = 40)$ data do not fully exclude a combination of dragging effects mixed with DR. Thus, as an additional quantitative test, we have converted the measured $\alpha_{mb}(\xi = 40)$ to a model of the rate coefficient expected at the lower expansion factor $\alpha''_{mb}(\xi = 20)$. A real DR resonance, as opposed to a dragging effect, should appear similar in both the converted $\alpha''_{mb}(\xi = 20)$ and the measured $\alpha_{mb}(\xi = 20)$. To generate $\alpha''_{mb}(\xi = 20)$ we deconvolved the $\alpha_{mb}(\xi = 40)$ data using the corresponding energy distribution $f_{mb}(\xi = 40)$ and the fitting procedure described in Section 3.4.3. We then reconvolved the extracted cross section with $f_{mb}(\xi = 20)$ to obtain the model of the experimental rate coefficient $\alpha''_{mb}(\xi = 20)$.

Figure 4 compares the measured rate coefficient $\alpha_{mb}(\xi = 20)$ and the converted $\alpha''_{mb}(\xi = 20)$. The measured $\alpha_{mb}(\xi = 40)$ and the corresponding model $\alpha'_{mb}(\xi = 40)$ are also displayed. We find satisfying agreement between $\alpha_{mb}(\xi = 20)$ and $\alpha''_{mb}(\xi = 20)$. The small differences remaining are attributed, in part, to uncertainties in the scaling used to derive $k_B T_\perp$ for $\xi = 40$ from that at $\xi = 20$. To first order we expect $k_B T_\perp$ to scale as ξ^{-1}, but there may be small nonlinear terms that we have ignored. These terms may introduce uncertainties in the $f_{mb}(\xi = 40)$ used which could carry over into the extracted cross section and finally into $\alpha''_{mb}(\xi = 20)$. Additionally, we did not measure $\alpha_{mb}(\xi = 40)$ at energies of $E_d > 20$ meV, so above this point we have used the $\alpha_{mb}(\xi = 20)$ data which may produce small discrepancies at energies $E_d \gtrsim 10$ meV.

4.2. Recombination Cross Section

We have converted the experimental DR rate coefficient $\alpha_{mb}(\xi = 20)$ to a cross section using a procedure introduced in Section 3.4.3 and described in detail in the Appendix. The resulting $\sigma'(E)$ is plotted in Figure 5 for the energy range $E = 0$–4.5 eV. These data are also given in tabular form in Table 2. The lower edge of the first energy bin is set to $E = 0$ and is not displayed on the logarithmic energy scale of the plot.

Deriving the cross section involves fitting α_{mb} with a sum of model rate coefficients, each convolved using a single cross-section bin. These sub-functions, $\sigma'_i \Psi_i(E_d)$, are plotted in Figure 3. We plot the corresponding collision energy distribution function f_{mb} for several values of E_d in Figure 6. To ensure physically meaningful results, we limited the fitting parameters σ'_i to positive values only. The fitting yielded a minimum $\chi^2/N_{DF} = 1.02$, where $N_{DF} = 30$ is the number of degrees of freedom in the fit.

To explore the numerical stability of the fitting, we have derived the cross section from a set of 1000 simulated merged beams spectra α^{sim}_{mb}. Each data point in a given simulated

Table 2
Cross Section σ for DR of HCl^+

E_{center} (eV)	E_{width} (eV)	σ (cm^2)	U^{lo}_{stat} (cm^2)	U^{hi}_{stat} (cm^2)	U^{lo}_{syst} (cm^2)	U^{hi}_{syst} (cm^2)
4.11(−5)	8.22(−5)	1.06(−11)	−4.01(−12)	+4.72(−12)	−1.57(−12)	+2.44(−12)
1.68(−4)	1.72(−4)	3.93(−12)	−1.37(−12)	+1.30(−12)	−7.11(−13)	+6.36(−13)
4.38(−4)	3.67(−4)	2.58(−12)	−2.93(−13)	+2.83(−13)	−4.25(−13)	+5.74(−13)
9.95(−4)	7.47(−4)	7.96(−13)	−5.71(−14)	+5.37(−14)	−1.30(−13)	+1.41(−13)
2.00(−3)	1.27(−3)	2.09(−13)	−1.58(−14)	+1.73(−14)	−2.93(−14)	+3.12(−14)
3.34(−3)	1.40(−3)	9.76(−14)	−1.05(−14)	+9.87(−15)	−1.34(−14)	+1.24(−14)
4.80(−3)	1.53(−3)	7.26(−14)	−7.22(−15)	+6.96(−15)	−9.92(−15)	+1.24(−14)
6.40(−3)	1.67(−3)	3.12(−14)	−2.79(−15)	+2.90(−15)	−6.08(−15)	+4.16(−15)
8.14(−3)	1.80(−3)	2.11(−14)	−1.76(−15)	+1.77(−15)	−2.65(−15)	+3.13(−15)
1.00(−2)	1.93(−3)	1.38(−14)	−1.38(−15)	+1.26(−15)	−2.15(−15)	+1.76(−15)
1.20(−2)	2.07(−3)	9.14(−15)	−1.18(−15)	+1.25(−15)	−1.16(−15)	+1.60(−15)
1.41(−2)	2.20(−3)	5.46(−15)	−1.09(−15)	+1.03(−15)	−1.37(−15)	+6.81(−16)
1.64(−2)	2.34(−3)	4.50(−15)	−1.08(−15)	+1.06(−15)	−5.63(−16)	+9.45(−16)
1.88(−2)	2.47(−3)	2.52(−15)	−9.71(−16)	+1.01(−15)	−6.19(−16)	+3.16(−16)
2.13(−2)	2.61(−3)	2.74(−15)	−8.99(−16)	+8.60(−16)	−3.39(−16)	+4.66(−16)
2.40(−2)	2.76(−3)	1.17(−15)	−6.68(−16)	+7.78(−16)	−2.48(−16)	+1.56(−16)
2.70(−2)	3.17(−3)	2.00(−15)	−7.12(−16)	+6.15(−16)	−2.48(−16)	+2.42(−16)
3.04(−2)	3.61(−3)	1.56(−15)	−5.30(−16)	+5.20(−16)	−2.06(−16)	+3.16(−16)
3.42(−2)	4.11(−3)	4.87(−16)	−3.25(−16)	+4.94(−16)	−2.24(−16)	+1.23(−16)
3.86(−2)	4.68(−3)	1.43(−15)	−4.14(−16)	+4.04(−16)	−1.79(−16)	+2.47(−16)
4.37(−2)	5.34(−3)	8.28(−16)	−3.17(−16)	+3.16(−16)	−1.53(−16)	+1.01(−16)
4.94(−2)	6.10(−3)	1.04(−15)	−2.66(−16)	+2.90(−16)	−1.25(−16)	+1.65(−16)
5.59(−2)	6.99(−3)	5.03(−16)	−1.68(−16)	+1.64(−16)	−6.54(−17)	+6.06(−17)
6.34(−2)	8.04(−3)	3.85(−16)	−1.36(−16)	+1.34(−16)	−5.67(−17)	+4.66(−17)
7.21(−2)	9.27(−3)	5.77(−16)	−1.29(−16)	+1.33(−16)	−6.93(−17)	+6.94(−17)
8.21(−2)	1.07(−2)	5.59(−16)	−1.13(−16)	+1.13(−16)	−6.80(−17)	+7.65(−17)
9.37(−2)	1.25(−2)	1.69(−16)	−1.05(−16)	+1.38(−16)	−2.03(−17)	+2.09(−17)
1.08(−1)	1.56(−2)	1.61(−16)	−8.57(−17)	+8.94(−17)	−1.94(−17)	+1.95(−17)
1.25(−1)	1.79(−2)	2.19(−16)	−1.01(−16)	+9.69(−17)	−2.74(−17)	+2.68(−17)
1.44(−1)	2.14(−2)	2.72(−16)	−7.82(−17)	+7.19(−17)	−3.28(−17)	+3.27(−17)
1.68(−1)	2.58(−2)	2.71(−16)	−7.67(−17)	+7.47(−17)	−3.25(−17)	+3.25(−17)
1.96(−1)	3.14(−2)	2.27(−16)	−7.02(−17)	+7.46(−17)	−2.73(−17)	+2.73(−17)
2.31(−1)	3.81(−2)	1.53(−16)	−6.10(−17)	+5.90(−17)	−1.84(−17)	+1.83(−17)
2.73(−1)	4.58(−2)	3.33(−17)	−2.49(−17)	+6.86(−17)	−1.16(−17)	+1.18(−17)
3.23(−1)	5.49(−2)	1.16(−16)	−5.75(−17)	+6.35(−17)	−1.41(−17)	+1.41(−17)
3.84(−1)	6.61(−2)	5.35(−17)	−3.70(−17)	+6.46(−17)	−8.89(−18)	+9.05(−18)
4.57(−1)	8.01(−2)	1.25(−16)	−5.76(−17)	+5.73(−17)	−1.53(−17)	+1.53(−17)
5.46(−1)	9.76(−2)	2.37(−17)	−1.80(−17)	+4.98(−17)	−8.58(−18)	+8.71(−18)
6.55(−1)	1.20(−1)	1.20(−17)	−8.68(−18)	+5.59(−17)	−1.38(−17)	+1.39(−17)
7.89(−1)	1.49(−1)	6.36(−17)	−3.76(−17)	+4.13(−17)	−7.74(−18)	+7.71(−18)
9.57(−1)	1.87(−1)	6.11(−17)	−3.22(−17)	+3.29(−17)	−7.35(−18)	+7.35(−18)
1.17(+0)	2.38(−1)	4.60(−17)	−2.84(−17)	+3.22(−17)	−5.55(−18)	+5.57(−18)
1.44(+0)	3.07(−1)	3.98(−17)	−2.58(−17)	+3.45(−17)	−5.12(−18)	+5.12(−18)
1.79(+0)	3.90(−1)	8.88(−17)	−3.60(−17)	+3.95(−17)	−1.07(−17)	+1.07(−17)
2.22(+0)	4.77(−1)	3.21(−17)	−2.12(−17)	+3.86(−17)	−6.75(−18)	+6.76(−18)
2.75(+0)	5.70(−1)	3.82(−17)	−2.48(−17)	+3.00(−17)	−4.78(−18)	+4.79(−18)
3.37(+0)	6.70(−1)	8.93(−17)	−2.76(−17)	+2.97(−17)	−1.08(−17)	+1.08(−17)
4.32(+0)	1.24(+0)	1.02(−16)	−2.64(−17)	+2.49(−17)	−1.23(−17)	+1.23(−17)

Notes. The binned cross section σ is given as a function of bin energy center E_{center}. Also listed is the energy width E_{width} of each bin. The asymmetric statistical and systematic uncertainties are given by U_{stat} and U_{syst}, respectively. The superscripts "lo" and "hi" give the lower and upper limits for the corresponding uncertainties. The total systematic error in the table includes the 12% scaling error and the uncertainties from $k_B T_\perp$ and $k_B T_\parallel$ (see text). The format $x(y)$ signifies $x \times 10^y$.

spectrum was obtained from the sum of the experimental value $\alpha_{mb}(E_d)$ and an additive shift which was randomly chosen from a Gaussian distribution centered around zero and with a width equal to the 1σ statistical error in $\alpha_{mb}(E_d)$. Each α^{sim}_{mb} was then fitted to derive a cross section. The cross-section values in each energy bin nearly follow a normal distribution. In some bins, however, up to 8% of the fitted σ_i values converged to zero. We attribute this behavior to the numerical instability for some of the fits, possibly due to converging to a local χ^2 minimum or because of strong correlations with cross-section values in neighboring energy bins. The mean cross-section values for each bin are displayed in Figure 5. The standard deviations above and below the mean are displayed by asymmetric vertical error bars and reflect the statistical errors propagated from α_{mb}. The mean cross-section values differ from those obtained directly from the experimental data by only a small fraction of the standard deviations. To test the accuracy of the mean cross section, we have convolved it using Equation (6) to generate a merged

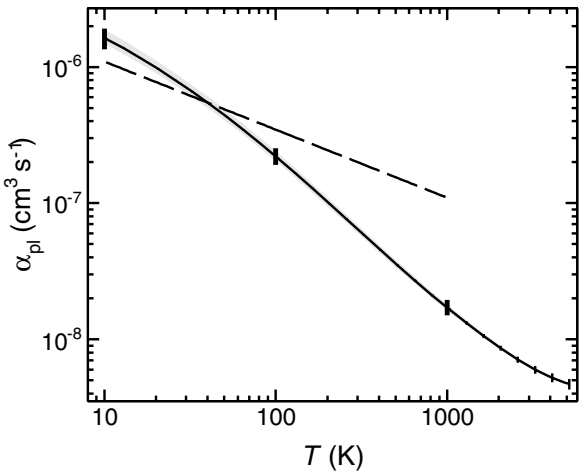

Figure 7. Experimentally derived DR plasma rate coefficient for HCl^+ shown by the solid line. The thin error bars display the statistical uncertainties in α_{mb} propagated through our method to generate a plasma rate coefficient. These error bars are only visible above ~1000 K. The thick error bars mark the total systematic uncertainty originating from the error on the absolute scaling and from the error due to uncertainties on $k_B T_\perp$ and $k_B T_\parallel$. The gray area shows the error originating solely from uncertainties in $k_B T_\perp$ and $k_B T_\parallel$. The dashed line shows α_{pl}^{di}, the rate coefficient typically assumed for diatomic molecular ions. The internal excitation temperature of the HCl^+ ions in this experiment lies near 300 K.

beam rate coefficient and compared the result to α'_{mb}, which was derived by fitting the experimental data. The difference between the two is less than a fifth of the statistical uncertainties in our experimental data.

Additionally, we have investigated the sensitivity of the cross section to the uncertainties in $k_B T_\perp$ and $k_B T_\parallel$. We have used their extreme values $k_B T_\perp = 1.3$–2.0 meV and $k_B T_\parallel = 20$–$70\,\mu$eV to generate f_{mb} and derived the cross section from the 1000 model rate coefficients, as discussed above. The mean cross sections were then compared to the one obtained with the most probable electron beam temperatures $k_B T_\perp = 1.65$ meV and $k_B T_\parallel = 25\,\mu$eV. The differences originating from $k_B T_\perp$ and $k_B T_\parallel$ were added in quadrature and are displayed by gray bars in Figure 5. The sensitivity of $\sigma'(E)$ to the electron beam parameters generally decreases with increasing energy. This is due to the decreasing relative energy spread $\Delta E/E$ with increasing energy. There is, though, an enhancement of the sensitivity seen in a few bins at $E \sim 0.03$ eV. We attribute this to narrow structures in the cross section with spacing comparable to the energy resolution at these energies (of the order of 2.5 meV). The effect of the electron beam temperature parameters is significantly lower than the statistical errors at all energies. Last, the 12% uncertainty on the absolute scaling of α_{mb} directly propagates to σ'. However, this error is too small to be seen in Figure 5.

4.3. Plasma Recombination Rate Coefficient

We have used the model cross section σ' as a representation of the DR cross section σ and converted it to a plasma rate coefficient using the procedures described in Section 3.4.4. The resulting $\alpha_{pl}(T)$ is plotted in Figure 7 for a plasma temperature range $T = 10$–5000 K.

To propagate the statistical uncertainty from the measured α_{mb} to the derived α_{pl}, we follow the technique used for the cross section in Section 4.2. First we created a set of 1000 simulated merged beams spectra α_{mb}^{sim} based on the measured α_{mb} and the corresponding statistical uncertainty. Each α_{mb}^{sim} was used to derive a cross section which was subsequently convolved with vf_{pl} to generate a plasma rate coefficient α_{pl}^{sim}. The spread in the values of α_{pl}^{sim} at each T closely followed a normal distribution. The Gaussian width of this spread at each T was taken as the 1σ statistical accuracy for α_{pl}. For T below 400 K these errors are less than 1%. They increase at higher temperatures and reach 8% at 5000 K.

The uncertainties in $k_B T_\perp$ and $k_B T_\parallel$ introduce an error in the derived α_{pl}. The plasma rate coefficient displayed in Figure 7 was derived for $k_B T_\perp = 1.65$ meV. We have also evaluated α_{pl} taking into account the ± 0.35 meV uncertainty in $k_B T_\perp$ and repeated the analysis using the limiting values of $k_B T_\perp$. The corresponding respective change of α_{pl} is $\pm 12\%$ at $T = 10$ K, decreases to $\pm 8\%$ at 100 K, and is less than $\pm 5\%$ above 1000 K. Varying $k_B T_\parallel$ within the estimated range of values has a much smaller effect. At $T = 10$ K the change in α_{pl} is $^{+3.5}_{-0.5}\%$ and drops to less than $^{+0.5}_{-0.1}\%$ at $T \geqslant 50K$. In this paragraph, positive (negative) changes in α_{pl} correspond to increased (decreased) $k_B T_\parallel$ and $k_B T_\parallel$.

The only other important systematic uncertainty in α_{pl} is the 12% absolute scaling error propagated from α_{mb}. We treat this scaling error and those from $k_B T_\perp$ and $k_B T_\parallel$ as independent and add them in quadrature. The resulting total systematic error amounts to 17% at 10 K, 14% at 100 K, and less than 13% above 1000 K.

We have fitted our results for ease of use in astrochemical models. We found that neither the two-parameter function commonly used to describe DR plasma rate coefficients (e.g., Florescu-Mitchell & Mitchell 2006) nor the more general three-parameter extension used in astrochemical databases (e.g., Woodall et al. 2007; Wakelam et al. 2012) are able to fit our measured plasma rate coefficient accurately over the entire temperature range from 10 to 5000 K. Such fits do not reproduce our results to within better than 40%. Therefore we propose a modified form of the two-parameter function, namely

$$\alpha_{pl}^{fit}(T) = A \left(\frac{300}{T}\right)^n + B, \tag{11}$$

where

$$B = T^{-3/2} \sum_{i=1}^{4} c_i \exp(-T_i/T). \tag{12}$$

This new function allows for more accurate fits than the previously used fitting functions. The results of fitting Equation (11) to our data over the full temperature range are given in Table 3. The deviations of α_{pl}^{fit} from the data are less than 1% over the full temperature range. It should be emphasized that the internal temperature of the HCl^+ ions in the experiment yielding these result is expected to lie near 300 K.

5. DISCUSSION

5.1. Comparison with Previous Analysis Methods

The principal difference between our new method for deriving the cross section and the plasma rate coefficient compared to the methods used in previous merged beams DR measurements lies in the conversion of the merged beams rate coefficient to a cross section. Our new method is essentially a one-step process. The traditional method requires two steps: first, it corrects the merged beams rate coefficient for the increased electron–ion

Table 3
Fit Parameters for HCl^+ DR Plasma Rate Coefficient α_{pl} Using Equation (11)

Parameter	Value		Unit
	x	y	
A	1.33(4)	−8	$cm^3\ s^{-1}$
n	3.7(1)	−1	Dimensionless
c_1	5.95(4)	−4	$K^{3/2}\ cm^3\ s^{-1}$
c_2	1.72(8)	−4	$K^{3/2}\ cm^3\ s^{-1}$
c_3	−4.59(4)	−4	$K^{3/2}\ cm^3\ s^{-1}$
c_4	−5.3(9)	−4	$K^{3/2}\ cm^3\ s^{-1}$
T_1	9.2(2)	0	K
T_2	7.7(7)	1	K
T_3	8.89(2)	1	K
T_4	3.4(4)	3	K

Notes. The values in parentheses give the 1σ error for the least significant digit shown. The value for each parameter is given by $x \times 10^y$.

collision energy in the merging and de-merging regions while ignoring the electron velocity spread (Lampert et al. 1996) then the corrected rate coefficient is deconvolved to yield a cross section, assuming parallel beams in the interaction zone and zero electron energy spread along the beam axis, i.e., $k_B T_\parallel = 0$ (Mowat et al. 1995). Our approach allows us to estimate the errors arising from the assumptions for each of these two steps.

To test the validity of the approach from Lampert et al. (1996), we have extracted the cross section from α_{mb} using our new approach and converted it to α^*_{mb} using Equation (7). The resulting α^*_{mb} then represents the rate coefficient as it would be measured in a merged beams configuration with parallel beams only and no merging or de-merging sections. Next we have reanalyzed our measured α_{mb} data using the method of Lampert et al. (1996) to generate α^{*L}_{mb}. Comparing the two data sets, α^*_{mb} and α^{*L}_{mb}, at high energies, where $E_d \gtrsim k_B T_\perp$, our correction procedure and the one proposed by Lampert et al. (1996) are equal to within their statistical accuracies. However, at lower energies, the traditional correction results in a merged beams rate coefficient that is up to ∼5% higher. Both our toroid correction method and that of Lampert et al. increase the merged beams rate coefficient at these low energies. Therefore, the difference can be interpreted as an over-correction by the older approach. We attribute this difference to the neglected electron velocity spread in the Lampert et al. method.

Next we tested the combined effects of the Lampert et al. (1996) and the Mowat et al. (1995) steps. To do this, we employed our new method for the cross-section derivation with two modifications. First, we used α^{*L}_{mb} as the input rate coefficient, and second, we generated the collision energy distribution for straight beams f^*_{mb} while setting $k_B T_\parallel = 0$. This latter step simulates the Mowat et al. approximation. We then converted the extracted cross section to the plasma rate coefficient α^M_{pl} using Equation (10). The resulting plasma rate coefficient is larger than α_{pl} by 2.3% at $T = 10$ K, 4.2% at $T = 100$ K, and to 1.7% at $T = 1000$ K. The spread in these values due to the uncertainties in $k_B T_\parallel$ and $k_B T_\perp$ is less than ±0.9%.

The errors in α_{pl} for HCl^+ DR which are introduced by the Lampert et al. (1996) and Mowat et al. (1995) approximations are only a few percent, much smaller than the other systematic errors in the measurement. However, larger differences could potentially arise if the measured merged beams rate coefficient were highly structured or decreased more rapidly with increasing energy. Additionally, it is not trivial to implement a fast Fourier transform (FFT) method, such as recommended by Mowat et al. (1995), using DR data on a non-uniform energy grid. Furthermore, the FFT method does not weigh the input data points by their statistical importance. All of these issues are readily accounted for by our new approach. The advantages of our new method are likely to be critical for reliably analyzing the expected highly structured DR data from upcoming Cryogenic Storage Ring (CSR) experiments on rotationally cold molecular ions (von Hahn et al. 2011; Krantz et al. 2011).

5.2. Experimental DR Rate Coefficient

Up to $E_d \approx 0.5$ eV, the HCl^+ DR rate coefficient α_{mb} decreases rapidly with increasing energy. This behavior is typical for low-energy DR spectra (Florescu-Mitchell & Mitchell 2006; Larsson & Orel 2008) yet, as shown in Figure 3, the slope between $E_d = 4$ and 30 meV is much steeper than the rate coefficient derived from the $\sigma \propto E^{-1}$ expected for the direct DR process (Bates 1950; Larsson & Orel 2008). As described in Section 2, direct electron capture to a repulsive neutral potential surface is unlikely at these low collision energies. Thus, at these energies, DR is probably dominated by the indirect process and the enhanced rate coefficient most likely results from numerous DR resonances. These are unresolved due to both the energy resolution of the experiment and the natural widths of the resonances.

Based on the collision energies, these resonances probably originate from neutral Rydberg states converging to a rotationally excited HCl^+ $X\,^2\Pi$ core. The exact positions for the resonances cannot be easily determined because of the large number of combinations between the initial ∼300 K distribution of HCl^+ excited states and the many energetically accessible rovibrationally excited levels in the neutral Rydberg system. Still, the steep decrease of α_{mb} between $E_d = 4$–30 meV may be attributed to the rotational structure of HCl^+. As discussed in Section 2, each rotational level of the ion is expected to be the end point for a Rydberg DR resonance series. In Figure 3 we plot the range of such end point energies allowing for $\Delta J = 1$, 2, and 3 changes of the angular momentum with respect to the initial ionic state. The range of the end points (indicated by the gray bars) is due to the initial rotational excitation of the HCl^+ ions (using rotational parameters from Sheasley & Mathews 1973; the levels spacings are nearly the same for ions in the $X\,^2\Pi_{3/2}$ or $X\,^2\Pi_{1/2}$ state, respectively.) The energy range of the fastest decrease in α_{mb} matches best the lowest possible change of the angular momentum, i.e., $\Delta J = 1$. Thus, it appears likely that indirect processes involving rotational excitation of the ∼300 K HCl^+ ions play an important role for the DR rate at the lowest energies. Correspondingly, rotational excitation rates by low-energy electron collisions of HCl^+ may be large.

Somewhat more resolved structures appear between 30 and 300 meV. There is the suggestion of a neutral Rydberg series limit at ∼80 meV corresponding to the $3/2 \rightarrow 1/2$ HCl^+ fine-structure transition (Sheasley & Mathews 1973) and at ∼0.3 eV corresponding to the $v = 0 \rightarrow 1$ excitation (Linstrom & Mallard 2013). The structures are blurred partly by the energy resolution of the experiment and partly by the initial rotational distribution of the stored HCl^+ ions. Further interpretation cannot be given without more detailed calculations.

The increase in α_{mb} at $E_d \gtrsim 0.6$ eV can be attributed to opening of additional dissociation pathways forming either excited Cl (above 0.6 eV) or excited H (above 1.9 eV) or both. Moreover, Rydberg resonances involving the $A^2\Sigma^+$ electronically excited

HCl^+ core may also be present. Ion pair production, which can reduce the DR signal as discussed in Section 2, will set in above 1.7 eV. At these energies, the statistical uncertainties in our data prevent us from being able to discern the impact on the DR signal due to the opening up of these channels. DE channels are not accessible in the investigated collision energy range.

5.3. Cross Section

The derivation of the DR cross section from the merged beams rate coefficient makes the DR data independent of the experimental configuration. On the other hand, the experimental energy spread together with the statistical quality of the rate coefficient data limits the resolving power of our method for deriving the cross section. We have adjusted the cross-section binning such that it provides good energy resolution while keeping the numerical instabilities small. The interpretation of the derived cross section is therefore somewhat limited and one needs to proceed cautiously in interpreting any structures which have an energy width comparable to the energy binning. Given that caveat, much of the structure discussed above in $\alpha_{\rm mb}$ can also be seen in the cross section.

5.4. Plasma Rate Coefficient

Our experimentally derived DR plasma rate coefficient for HCl^+ displays an unusually steep slope. Existing astrochemical models usually approximate DR of HCl^+ by (Neufeld & Wolfire 2009)

$$\alpha_{\rm pl}^{\rm di} \approx 2.0 \times 10^{-7} \times (300/T)^{0.5}\ {\rm cm^3\ s^{-1}}.$$

This is believed to correspond to DR of typical diatomic molecular ions (Florescu-Mitchell & Mitchell 2006). However, some astrochemical databases use a value 1.5 times higher for HCl^+ (e.g., Woodall et al. 2007), though there is no obvious reason for this. Taking the ratio of $\alpha_{\rm pl}/\alpha_{\rm pl}^{\rm di}$ yields 1.5, 1.1, 0.64, 0.33, and 0.16 at $T = 10, 30, 100, 300$, and 1000 K, respectively. Such differences are larger than our experimental error bars. Thus we find that the "typical" diatomic DR rate coefficient is incorrect in both magnitude and temperature dependence for HCl^+. Note, however, that our derived rate coefficient is for an internal temperature of ~300 K of the HCl^+ ions.

5.5. Astrochemical Implications

Our new data suggest that HCl^+ depletion by DR in the cold ISM (~10–50 K) is faster than or similar to that currently assumed in existing astrochemical models. However, at higher temperatures the new data display a slower HCl^+ destruction by DR. As HCl^+ leads to the formation of H_2Cl^+, the H_2Cl^+ abundance will also decrease or increase when using our new data, depending on the temperature. Unfortunately, the kinetic temperatures of the observed environments were not directly derived in the works of Lis et al. (2010), De Luca et al. (2012), and Neufeld et al. (2012). Model calculations (Neufeld & Wolfire 2009) predict that there is an abundance maximum of HCl^+ in the outer parts of dark interstellar clouds which, at an opacity of $A_v \sim 1$, are less dense than the core and with a temperature of ~500 K are also hotter. In these regions, DR is predicted to clearly dominate the destruction of HCl^+. Thus, our measured DR rate coefficient (which is about a factor of four lower than the ones used in current astrochemical models) will augment the predicted HCl^+ abundances in that region, leading to an improved agreement with the observed HCl^+ densities. It will also affect the H_2Cl^+ abundance in the outer parts of the clouds (which also predicted an abundance maximum at roughly the same cloud density as the one for HCl^+ is found), since a lesser efficient competition by the DR of HCl^+ will allow more H_2Cl^+ to be formed by reaction of HCl^+ with H_2.

Neufeld et al. (2012) have explored the effect of lowering the HCl^+ DR rate coefficient on the discrepancy between the predicted and observed HCl^+ and H_2Cl^+ abundances. In their astrochemical model they decreased $\alpha_{\rm pl}$ of HCl^+ to $\alpha_{\rm pl}^{\rm di}/10$. The resulting abundances of HCl^+ and H_2Cl^+ increased by factors of 2.7 and 1.3, respectively. In both cases the calculated abundances are still far too low to match the greater than 10 times larger observed abundances. The result of their tests suggests that our new HCl^+ DR data, which are about four times smaller than $\alpha_{\rm pl}^{\rm di}$ at the relevant temperature, cannot fully explain the discrepancy between current astrochemical models and the observations. Still, our new data differ from $\alpha_{\rm pl}^{\rm di}$ not only in magnitude but also in temperature dependence. Therefore the test of Neufeld et al. (2012) does not directly describe the effect of our new DR data and their calculations should be repeated in order to fully evaluate the remaining discrepancy.

We also note that our experimental data are for HCl^+ rotationally excited to $T_{\rm rot} \sim 300$ K. In the cold ISM, however, the internal excitation is expected to be much lower. In the very low density environment in interstellar clouds, the collision rate is much lower than the typical radiative decay time (Spitzer 1978). Thus $T_{\rm rot}$ is generally even lower than the kinetic temperature T and most of the molecules are expected to be in their rotational ground state. The response of the DR rate coefficients to $T_{\rm rot}$ has not yet been studied systematically. The few existing studies on light ions find that the measured merged beams rate coefficient exhibits an increasingly rich resonant structures with decreasing $T_{\rm rot}$ (e.g., Amitay et al. 1996, Zhaunerchyk et al. 2007, Petrignani et al. 2011, Schwalm et al. 2011). This can be explained by the smaller number of rotational states that contribute with decreasing $T_{\rm rot}$. The individual resonant structures thereby become resolved as they no longer overlap with resonances of other, energetically higher states. Low values of $T_{\rm rot}$ can result in either a lower or higher plasma rate coefficient, depending on the particular shape of the cross section. We expect that future DR measurements at the CSR facility will be able to address this issue by investigating molecular ions rotationally colder than what can be achieved with TSR.

6. SUMMARY

We have measured the absolute DR rate coefficient for HCl^+ in a merged beams configuration at electron–ion collision energies from 0 eV to 4.5 eV. Using a novel method, we have converted the experimental merged beams rate coefficient to a cross-section and then to a plasma rate coefficient. Our new approach provides more precise results and better control on uncertainties as compared to previously used methods. At molecular cloud temperatures below ~50 K, the resulting plasma rate coefficient is similar or faster than that typically assumed for DR of other diatomic molecular ions. However, at higher temperatures relevant for HCl^+ observations, DR of HCl^+ is slower than previously expected. Thus our data indicate that the current issues in modeling chlorine chemistry in interstellar clouds may be partly resolved by our new DR data.

We thank the MPIK accelerator and TSR crews for their excellent support. O.N. and D.W.S. were supported in part by the NSF Division of Astronomical Sciences Astronomy and

Astrophysics Grants program and by the NASA Astronomy and Physics Research and Analysis Program. D.S. acknowledges support by the Weizmann Institute of Science through the Joseph Meyerhoff program. This work is supported in part by the German-Israeli Foundation for Scientific Research (GIF under contract nr. I-900-231.7/2005). W.G. acknowledges partial support by the COST Action CM0805: "The Chemical Cosmos: Understanding Chemistry in Astronomical Environments." B.Y. is grateful for the support from MPG and from the CAS-MPS program. This work is supported in part by the DFG Priority Program 1573 "Physics of the Interstellar Medium" and by the Max Planck Society.

APPENDIX

DECONVOLVING THE MEASURED MERGED BEAMS RATE COEFFICIENT

In Section 3.4.3 we briefly introduced a new method for deriving a cross section from the measured merged beams rate coefficient. This approach begins with a model cross section $\sigma'(E)$ which we multiply by the relative collision velocity and then, following Equation (6), convolve the product with the center-of-mass energy distribution function $f_{\rm mb}(E, E_{\rm d}, T_{||}, T_{\perp}, \boldsymbol{X})$. This generates a model rate coefficient $\alpha'_{\rm mb}(E_{\rm d})$. We iteratively modify the parameters defining the shape of $\sigma'(E)$ to minimize the χ^2 between the measured $\alpha_{\rm mb}(E_{\rm d})$ and the model $\alpha'_{\rm mb}(E_{\rm d})$. In this Appendix, we discuss the core of our deconvolution method, namely the numerical evaluation of Equation (6).

The required collision energy distribution $f_{\rm mb}(E, E_{\rm d}, T_{||}, T_{\perp}, \boldsymbol{X})$ is not known in analytical form. So we use a Monte Carlo simulation that includes the effects of both the electron velocity spread and the beam overlap geometry. The Monte Carlo method requires a large number of simulated events to reach a low statistical uncertainty for the multidimensional $f_{\rm mb}$. The resulting computational demands rise steeply with the power of the number of dimensions. This can be partly reduced by fixing the electron energy spreads $k_{\rm B}T_{||}$ and $k_{\rm B}T_{\perp}$ and also fixing the merged beams geometry $\boldsymbol{X}$, as none of these parameters change during the measurement and can thus be kept constant during the fit.

The required computational time can be further reduced by using a good discretization of the E dimension. We model $\sigma'(E)$ as a histogram with non-uniform bin widths. For $E \lesssim k_{\rm B}T_{\perp}$, we choose bin widths similar to the experimental energy resolution for $E = E_{\rm d}$. At higher energies we use broader bins, but which are still much narrower than the structure typically observed in TSR DR measurements of $\alpha_{\rm mb}(E_{\rm d})$. A consequence and advantage of this approach is that the exact energy bin positions and widths are not critical and can be fixed during fitting without any significant loss in the precision of the fit.

With a fixed energy binning we can then transform the model form of Equation (6) into the summation

$$\alpha'_{\rm mb}(E_{\rm d}) = \sum_i \sigma'_i \int_{E_i}^{E_{i+1}} v\, f_{\rm mb}(E, E_{\rm d}, T_{||}, T_{\perp}, \boldsymbol{X})\, dE, \quad \text{(A1)}$$

where σ'_i is the model cross section in the ith energy bin and E_i and E_{i+1} are the edges of the bin. Defining the function

$$\Psi_i(E_{\rm d}, T_{||}, T_{\perp}, \boldsymbol{X}) \equiv \int_{E_i}^{E_{i+1}} v\, f_{\rm mb}(E, E_{\rm d}, T_{||}, T_{\perp}, \boldsymbol{X})\, dE, \quad \text{(A2)}$$

we can re-express Equation (A1) as

$$\alpha'_{\rm mb}(E_{\rm d}) = \sum_i \sigma'_i\, \Psi_i(E_{\rm d}, T_{||}, T_{\perp}, \boldsymbol{X}). \quad \text{(A3)}$$

Because the Ψ_i integrals are independent of the fitting parameters σ'_i, the integrals can be calculated prior to the iterative χ^2-minimization procedure. As a result, the overall fitting time is reduced and is dominated by the initial generation of the Ψ_i integrals. For a given required statistical accuracy, this scales linearly with number of cross-section bins σ'_i and with the number of fitted energy points $E_{\rm d}$. Additionally, because the form of Equation (A3) is a linear combination of the constant factors Ψ_i scaled by the fitting parameters σ'_i, it allows us to use efficient fitting algorithms (e.g., Press et al. 2007).

We calculate the Ψ_i integrals employing a numerical Monte Carlo method (e.g., Press et al. 2007). In short, we use a model of the merged beams geometry in which we generate a large number of collision events according to the fixed experimental parameters $E_{\rm d}$, $T_{||}$, $T_{\perp}$, and $\boldsymbol{X}$. Events are generated by randomly selecting the dissociation position in $\boldsymbol{X}$ as well as the electron velocity vector for the given values of $E_{\rm d}$, $T_{||}$ and $T_{\perp}$. The exact probability distributions used are discussed below.

For each event j, we calculate the electron–ion collision velocity v_j and the corresponding center-of-mass collision energy E_j. The propagation through the model of the randomized dissociation position and electron velocity vector ensures that the set of values generated for E_j follows the desired $f_{\rm mb}(E)$ distribution. Hence the numerical integration of Equation (A2) reduces to a simple summation given by

$$\Psi_i(E_{\rm d}, T_{||}, T_{\perp}, \boldsymbol{X}) = \frac{1}{N_{\rm s}} \sum_{j=1}^{N_{\rm s}} \begin{cases} v_j, & E_i \leqslant E_j < E_{i+1} \\ 0, & \text{otherwise} \end{cases}, \quad \text{(A4)}$$

where $N_{\rm s}$ is the total number of simulated events. For each energy $E_{\rm d}$, we generate $N_{\rm s} = 10^7$ events. This provides a statistical precision better than $\sim$0.1% for the resulting $\alpha'_{\rm mb}(E_{\rm d})$. The fitting sub-functions $\sigma_i\Psi_i(E_{\rm d})$ are shown in Figure 3.

Although not directly needed for the cross-section derivation, one can similarly obtain an average value of the distribution function $f_{\rm mb}$ in energy bin i as

$$f_{{\rm mb},i}(E_{\rm d}, T_{||}, T_{\perp}, \boldsymbol{X}) = \frac{1}{N_{\rm s}} \sum_{j=1}^{N_{\rm s}} \begin{cases} 1, & E_i \leqslant E_j < E_{i+1} \\ 0, & \text{otherwise} \end{cases}. \quad \text{(A5)}$$

The histograms $f_{{\rm mb},i}$ are plotted in Figure 6 for several values of $E_{\rm d}$. Here we have chosen a very narrow energy binning so that the histogram $f_{{\rm mb},i}$ closely approximates $f_{\rm mb}$. For comparison, we also plot in Figure 6 the energy distribution function for parallel beams $f^*_{\rm mb}$. This helps to highlight the extension of the high-energy tail $f_{\rm mb}$ due to the merging and demerging of the beams.

We model the electron beam as a cylindrical body with the shape described in Section 3.1. Given that the ion beam diameter is much smaller than the electron beam and that the magnetic fields in the Target are too weak to significantly affect the ions, we can approximate the ion beam as a straight line of zero diameter. We assume uniform electron and ion beam densities within the model beams and can therefore treat the event probability distribution as uniform over the entire interaction region.

Because of the large difference between the electron and ion masses and the phase-space cooling, the velocity spread of the cooled ion beam has a negligible effect on the experimental energy spread $f_{\rm mb}$. Thus we can model the ions with a constant laboratory velocity of $v_{\rm i} = \sqrt{2E_{\rm cool}/m_e}$ with no velocity spread. The electron velocity vectors are randomized in the laboratory frame. The orientation of the electron beam bulk velocity is determined from the electron beam geometry at the position of each simulated event. The velocity components perpendicular to the electron beam axis are described by a Gaussian distribution centered around $v_{e,\perp} = 0$ and with a width of $\sigma_\perp = \sqrt{k_{\rm B}T_\perp/m_e}$. In the parallel direction, the velocity distribution is centered at $v_{e,\parallel} = v_{\rm i} + \sqrt{2E_{\rm d}/m_e}$ with a Gaussian width of $\sigma_\parallel = \sqrt{k_{\rm B}T_{||}/m_e}$. The electron–ion collision velocity v_j is obtained by subtracting the ion and electron velocity vectors. The corresponding energy E_j is then used for the summation condition in Equation (A4) to decide to which Ψ_i each event j contributes.

Lastly, we note that choosing an appropriate energy binning for the model cross section is essential in order to avoid numerical instabilities when fitting the model $\alpha'_{\rm mb}$ to the measured $\alpha_{\rm mb}$. Bins significantly narrower than the energy resolution or than the energy spacing between the measured data points give an under-determined fitting system which results in fitted σ'_i values with large uncertainties strongly correlated with neighboring bins. On the other hand, using bins which are too broad results in too coarse of a fitting function and a poorer quality of the fit.

We have developed a general recipe to define an optimal cross-section energy binning which does not suffer from these effects. The bins are defined at lower energies starting with the lower energy edge of the first bin set to 0 eV, and the upper edge to $\sim k_{\rm B}T_\perp/20$. The edges of subsequent bins are set to $E_{i+1} = E_i + \delta E$. At energies $E_i < k_{\rm B}T_\perp$ we set the step to $\delta E \approx E_i$. At higher energies we set the bin width to be approximately the energy resolution ΔE given by Equation (8). This is motivated by the fact that structures in the cross section which are separated by less than $\sim \Delta E$ can not be resolved. For energies $E_{\rm d} \gg \Delta E$ the spacing $\Delta E_{\rm d}$ between the measured $\alpha_{\rm mb}$ points is often larger than ΔE. For these cases we set the σ_i bin edges to fall between the measurement points, i.e., $E_i = (E_{{\rm d},i} + E_{{\rm d},i+1})/2$, so that each point in $\alpha_{\rm mb}$ effectively contributes to only one cross-section bin.

The binning generated by this method was tested on several DR spectra from previous TSR measurements for other systems. In all cases a high-quality fit was achieved with reasonable numerical stability. The remaining errors, due to residual numerical instabilities, basically integrate away when calculating the plasma rate coefficient $\alpha_{\rm pl}$ using Equation (10). As a result, the dominant error in $\alpha_{\rm pl}$ is due to the statistical and systematic errors in $\alpha_{\rm mb}$ and the uncertainties in $k_{\rm B}T_\perp$ and $k_{\rm B}T_\parallel$. The resulting uncertainty as it relates to our HCl^+ results are discussed in Section 4.

REFERENCES

Alexander, M. H., Li, X., Liyanage, R., & Gordon, R. J. 1998, CP, 231, 331
Amin, M. Y. 1996, EM&P, 73, 133
Amitay, Z., Zajfman, D., & Forck, P. 1994, PhRvA, 50, 2304
Amitay, Z., Zajfman, D., Forck, P., et al. 1996, PhRvA, 54, 4032
Andersen, L. H., Hvelplund, P., Knudsen, H., & Kvistgaard, P. 1989, PhRvL, 62, 2656
Bates, D. R. 1950, PhRv, 78, 492
Bettendorff, M., Peyerimhoff, S. D., & Buenker, R. J. 1982, CP, 66, 261
Blake, G. A., Anicich, V. G., & Huntress, W. T. 1986, ApJ, 300, 415
Cheng, M., Brown, J. M., Rosmus, P., et al. 2007, PhRvA, 75, 012502
Dalgarno, A., & Black, J. H. 1976, RPPh, 39, 573
Dalgarno, A., de Jong, T., Oppenheimer, M., & Black, J. H. 1974, ApJL, 192, L37
Danared, H. 1993, NIMPA, 335, 397
De Luca, M., Gupta, H., Neufeld, D., et al. 2012, ApJL, 751, L37
Federman, S. R., Cardell, J. A., van Dishoeck, E. F., Lambert, D. L., & Black, J. H. 1995, ApJ, 445, 325
Fischer, C. F., & Tachiev, G. 2013, MCHF/MCDHF Collection, Version 2, 35, available online at http://physics.nist.gov/mchf
Florescu-Mitchell, A., & Mitchell, J. 2006, PhR, 430, 277
Habs, D., Baumann, W., Berger, J., et al. 1989, NIMPB, 43, 390
Hochadel, B., Albrecht, F., Grieser, M., et al. 1994, NIMPA, 343, 401
Jura, M. 1974, ApJL, 190, L33
Kilgus, G., Habs, D., Schwalm, D., et al. 1992, PhRvA, 46, 5730
Krantz, C., Berg, F., Blaum, K., et al. 2011, JPhCS, 300, 012010
Krantz, C., Orlov, D. A., Hoffmann, J., et al. 2009, JPhCS, 192, 012025
Krauss, M., & Julienne, P. S. 1973, ApJL, 183, L139
Lampert, A., Wolf, A., Habs, D., et al. 1996, PhRvA, 53, 1413
Larson, Å., Fonseca dos Santos, S., & Orel, A. E. 2012, BAPS, 57, 46
Larsson, M., & Orel, A. E. 2008, Dissociative Recombination of Molecular Ions (Cambridge: Cambridge Univ. Press)
Lefebvre-Brion, H., Liebermann, H. P., & Vázquez, G. J. 2011, JChPh, 134, 204104
Lestinsky, M., Lindroth, E., Orlov, D. A., et al. 2008, PhRvL, 100, 033001
Linstrom, P., & Mallard, W. (eds.) 2013, in NIST Chemistry WebBook, NIST Standard Reference Database Number 69 (Gaithersburg, MD: National Institute of Standards and Technology), 20899, http://webbook.nist.gov
Lis, D. C., Pearson, J. C., Neufeld, D. A., et al. 2010, A&A, 521, L9
Liyanage, R., Yang, Y.-a., Hashimoto, S., Gordon, R. J., & Field, R. W. 1995, JChPh, 103, 6811
Long, J., Wang, H., & Kvaran, A. 2013, JChPh, 138, 044308
Mowat, J. R., Danared, H., Sundström, G., et al. 1995, PhRvL, 74, 50
Müller, A. 1999, RSPTA, 357, 1279
Neufeld, D. A., Roueff, E., Snell, R. L., et al. 2012, ApJ, 748, 37
Neufeld, D. A., & Wolfire, M. G. 2009, ApJ, 706, 1594
Novotný, O., Badnell, N. R., Bernhardt, D., et al. 2012, ApJ, 753, 57
Novotný, O., Buhr, H., Stützel, J., et al. 2010, JPCA, 114, 4870
Novotny, O., Mitchell, J. B. A., LeGarrec, J. L., et al. 2005, JPhB, 38, 1471
Novotný, O., Motapon, O., Berg, M. H., et al. 2009, JPhCS, 192, 012021
Orlov, D. A., Krantz, C., Wolf, A., et al. 2009, JAP, 106, 054907
Orlov, D. A., Sprenger, F., Lestinsky, M., et al. 2005, JPhCS, 4, 290
Orlov, D. A., Weigel, U., Schwalm, D., Terekhov, A. S., & Wolf, A. 2004, NIMPA, 532, 418
Peng, R., Yoshida, H., Chamberlin, R. A., et al. 2010, ApJ, 723, 218
Petrignani, A., Altevogt, S., Berg, M. H., et al. 2011, PhRvA, 83, 032711
Poth, H. 1990, PhR, 196, 135
Pradhan, A. D., Kirby, K. P., & Dalgarno, A. 1991, JChPh, 95, 9009
Press, W. H., Teukolsky, S. A., Vetterling, W. T., & Flannery, B. P. 2007, Numerical Recipes : The Art of Scientific Computing (3rd ed.; Cambridge: Cambridge Univ. Press)
Ralchenko, Y., Kramida, A., Reader, J., & NIST ASD Team., 2011, Atomic Spectra Database, Version 4.1.0 (Gaithersburg, MD: National Institute of Standards and Technology), http://physics.nist.gov/asd
Romanescu, C., & Loock, H.-P. 2007, JChPh, 127, 124304
Schippers, S., Schnell, M., Brandau, C., et al. 2004, A&A, 421, 7
Schwalm, D., Shafir, D., Novotny, S., et al. 2011, JPhCS, 300, 012006
Shafir, D., Novotny, S., Buhr, H., et al. 2009, PhRvL, 102, 223202
Sheasley, W. D., & Mathews, C. W. 1973, JMoSp, 47, 420
Sonnentrucker, P., Friedman, S. D., & York, D. G. 2006, ApJL, 650, L115
Spitzer, L. 1978, Physical Processes in the Interstellar Medium (New York: Wiley)
Sprenger, F. 2003, Dissertation, Univ. Heidelberg, http://www.ub.uni-heidelberg.de/archiv/4415
Sprenger, F., Lestinsky, M., Orlov, D. A., Schwalm, D., & Wolf, A. 2004, NIMPA, 532, 298
Steck, M., Bisoffi, G., Blum, M., et al. 1990, NIMPA, 287, 324
Stützel, J. 2011, Dissertation, Univ. Heidelberg, http://www.ub.uni-heidelberg.de/archiv/11597
von Hahn, R., Berg, F., Blaum, K., et al. 2011, NIMPB, 269, 2871
Waffeu Tamo, F. O., Buhr, H., Motapon, O., et al. 2011, PhRvA, 84, 022710
Wakelam, V., Herbst, E., Loison, J.-C., et al. 2012, ApJS, 199, 21
Wolf, A., Buhr, H., & Novotný, O. 2011, JPhCS, 300, 012008
Woodall, J., Agúndez, M., Markwick-Kemper, A. J., & Millar, T. J. 2007, A&A, 466, 1197
Zhaunerchyk, V., Al-Khalili, A., Thomas, R. D., et al. 2007, PhRvL, 99, 013201